Sensors & Actuators: A. Physical 394 (2025) 116966

Contents lists available at ScienceDirect

Sensors and Actuators: A. Physical

journal homepage: www.journals.elsevier.com/sensors-and-actuators-a-physical

Impact of the parasitic photothermal effect on the performance of an optomechanical nanoantenna for NIR radiation detection

Daniyal Khosh Maram *, Joan Garcia-Garcia, Xavier Cartoixà, Gabriel Abadal

Departament d'Enginyeria Electrònica, Universitat Autònoma de Barcelona, 08193 Bellaterra, Barcelona, Spain

ARTICLE INFO

Keywords:
Optomechanical nanoantennas
Near-infrared (NIR) radiation detection
Opto-thermomechanical transduction
Opto-electromechanical transduction
COMSOL Multiphysics simulations
Design optimization

ABSTRACT

This paper investigates the impact of the opto-thermomechanical (OTM) parasitic response of an optomechanical nanoantenna on the main opto-electromechanical (OEM) transduction mechanism involved in the near-infrared (NIR) radiation detection. Through comprehensive experimental and computational analyses, we have modelled how this parasitic effect overlaps with the desired opto-electromechanical response. Utilizing COMSOL Multiphysics, we have simulated thermal, optical, and mechanical interactions within the optomechanical structure. Our findings indicate that the parasitic OTM effect significantly influences the device's mechanical deflection, driven primarily by localized heating at the microcantilever's free end. Experimental data validates simulation results, demonstrating the parasitic response's dominance over the intended functionality. A figure of merit (FoM), defined as the ratio between the transducing OEM signal over the parasitic OTM response has been defined to quantify the performance of the optomechanical nanoantenna detector, as well as to propose geometry design improvements to optimize this performance.

1. Introduction

Micro Electro Mechanical Systems (MEMS) is a well stablished discipline that emerged as a cornerstone technology for a wide range of applications, leveraging their ability to integrate electrical and mechanical components at the microscale [1]. These systems rely on electromechanical transduction mechanisms, which convert signals and energy from the mechanical into the electrical domain and vice versa, to enable functionalities such as sensing [2], actuation [3], and energy harvesting [4]. Among the wide range of transduction mechanisms that make such conversion processes possible, thermal [5], piezoresistive [6], piezoelectric [7], electrostatic [8], and magnetomotive [9] are the most commonly used. Although MEMS technology has reached a level of maturity for long time now that allows us to find it in daily consumer electronics devices [10] or healthcare [11] and industrial [12] applications, new challenges such as MEMS computing [13], MEMS-based neurotechnology [14] or 3D-MEMS technology [15] are still being faced in the frontiers of this field.

In particular, RF-MEMS sub-technology initially devoted to the interaction of MEMS with electromagnetic radiofrequency (RF) radiation [16] is being extended in the recent years to the terahertz and optical domains to bring forward new applications in tuneable THz metamaterials [17], imaging [18] and uncooled IR detection [19].

In terms of signal reception, MEMS technology has also seen contributions from cutting edge examples such as the nanotube radio [20], where a single carbon nanotube was used as a mechanical antenna that integrated also the demodulator and the speaker of a complete AM reception system. Later, RF signal detection was also demonstrated with a much simpler mechanical antenna based on an unpolarized microcantilever [3] and the new mechanical antenna topic was born, inspired by Jensen's work, showing promising capabilities in the Low Frequency (LF) [21] and Very Low Frequency (VLF) [22] telecommunications.

In earlier research, R. Ruiz et al. [23–25] investigated a novel mechanical antenna concept called MEMSTENNA, that combined an antenna component with a resonant MEMS. Through the use of MEMSTENNA technology, radiofrequency electromagnetic energy can be directly converted to mechanical motion. C. Belacel et al. [26] applied the MEMSTENNA concept to the 1–10 THz frequency range and proposed a new type of THz detector that directly transforms electromagnetic signals into mechanical responses. The authors demonstrate the improvement in frequency response at room temperature of this THz detector by avoiding the thermal mechanisms commonly found in other types of THz bolometric detectors [27–29].

Very recently, a preliminary study of an extension of the

* Corresponding author.
E-mail address: daniyal.khoshmaram@uab.cat (D.K. Maram).

https://doi.org/10.1016/j.sna.2025.116966
Received 10 February 2025; Received in revised form 18 June 2025; Accepted 12 August 2025
Available online 13 August 2025
0924-4247/© 2025 The Author(s). Published by Elsevier B.V. This is an open access article under the CC BY-NC license (http://creativecommons.org/licenses/by-nc/4.0/).

MEMSTENNA concept to the optical domain has been published by the authors [30]. In that work, the design and fabrication process of a NIR NEMSTENNA, a combination of a dipole optical nanoantenna with commercial microcantilevers, was first presented. In that same work, a detailed analysis of the opto-electromechanical transduction mechanism was also reported, showing that such NEMSTENNAS exhibit mechanical responses in the 0.01–0.1 nm range, but the parasitic impact on the device performance of the thermally induced deflection of cantilevers by bimetallic effect was neglected and not included in the analysis. In this article, on the one hand, the opto-thermally induced deflection of the cantilevers has been calculated and validated experimentally in order to predict its effect on the opto-electromechanical signal. On the other hand, an improved version of the NEMSTENNA based on an optimized nanodipole geometry which maximizes the electrostatic transducing voltage in the feed gap of the nanoantenna has been designed. The article is organized in the following way: In Section 2, the opto-mechanical nanoantenna device (NEMSTENNA), which is a combination of a dipole nanoantenna integrated in the free end of two mechanical microcantilevers, is defined. It is also discussed how the device operates and the mechanisms that initiate transduction. Next, the nanoantenna's design is described in Section 3, along with results of the optimal geometry. In Section 4, we examine the COMSOL prediction of the mechanical response, which includes opto-electromechanical (OEM) and parasitic opto-thermomechanical (OTM) features. Finally, we also define the optomechanical nanoantenna design's Figure of Merit as the ratio between the transducing OEM signal over the parasitic OTM response, which highlights the importance of optimizing opto-mechanical responses over optothermal effects.

2. Device definition and working principle

The proposed optomechanical nanoantenna (NEMSTENNA) structure features a near-infrared (NIR) optical dipole nanoantenna, designed to resonate at a wavelength of 1.55 μm, integrated into one of the Au layers of two triangular Si_3N_4 microcantilevers at their free end, as shown in Fig. 1. The geometry of the dipole nanoantenna shown in Fig. 2, is defined by the length and width of its two components (L_1, L_2, W_1), as well as the dimensions of the supporting arms (L_{Arm1}, L_{Arm2}, W_2) that link the dipole components to the microcantilevers. Additionally, the thickness of the silicon nitride layer in the nanoantenna region is another critical design parameter that will have an important effect on the nanoantenna response, because this layer is the dielectric substrate that determine wave propagation velocity and dielectric losses. The two components of the dipole nanoantenna are positioned parallel to each other and separated by a gap distance, g_0, in the overlapping area located in the feed region of the antenna. In this feed gap area, an electrostatic transduction capacitance is created, which at the same time is electrically loading the nanoantenna. When the dipole nanoantenna is illuminated by a focused NIR laser beam with a wavelength of 1.55 μm (corresponding to a frequency of 193.41 THz), an alternating AC voltage, referred to as V_{gap}, is generated within the feed gap of the nanoantenna, as shown in Fig. 1(b). This voltage arises due to the interaction between the incoming radiation and the plasmonic properties of the optical nanoantenna. The generated AC voltage V_{gap}, which oscillates at the same frequency as the incident radiation, 193.41 THz in this case, induces an electrostatic force between the two components of the dipole nanoantenna which acts attracting the microcantilevers at their free end. Since this force depends quadratically on the inducing voltage, a DC component of the force and the consequent static deflection of the cantilevers are both produced. On the other hand, the AC component of the force, which oscillates at twice the frequency of the incident NIR radiation (hundreds of THz), will not induce any significant mechanical vibration of the microcantilevers because their natural vibration frequencies are 12 orders of magnitude lower (tens of kHz). This frequency mismatch ensures that the microcantilevers primarily respond to the DC component, maintaining stable mechanical operation without interference from high-frequency noise.

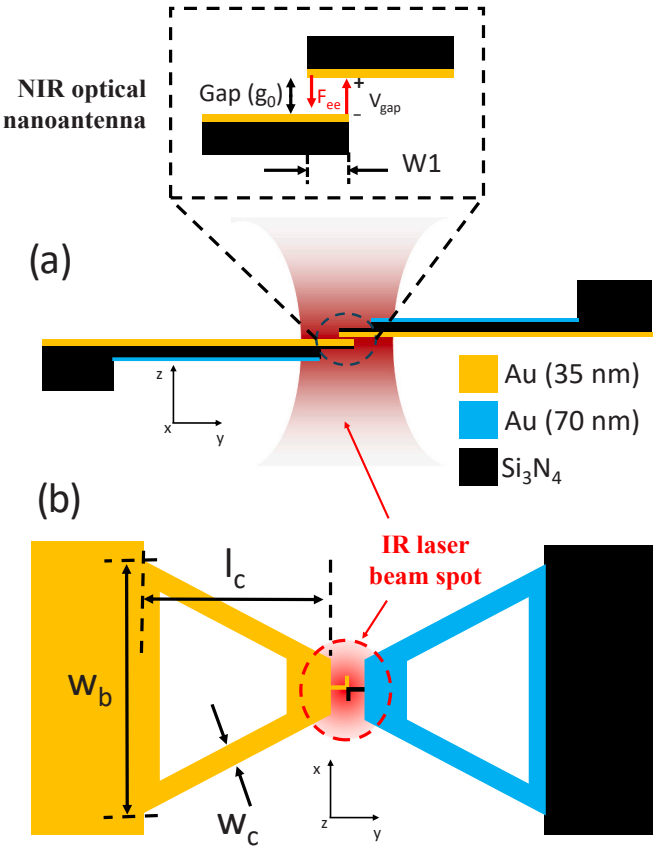

Fig. 1. Schematics of the lateral view (a) and top view (b) of the proposed optomechanical nanoantenna (NEMSTENNA) structure including the dipole NIR nano-antenna integrated at the free end of two microcantilevers, which is placed at the beam waist of a focused gaussian laser beam. In the zoom detail of the lateral view, voltage in the gap region, V_{gap}, induces an attractive electrostatic force, F_{ee}, on each optomechanical nanoantenna component.

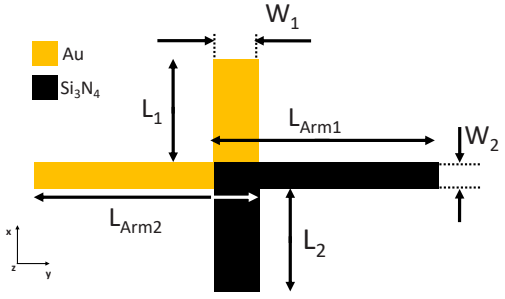

Fig. 2. Dipole nano-antenna layout with all dimensions that define its geometry.

3. Design of the nanoantenna

The electromagnetic resonance modes of a dipole nanoantenna are determined by its physical dimensions, and specially by its length. This section aims to investigate the relationship between dipole length and resonance occurrence, in terms of gap voltage and z-direction electric field in the nanoantenna feed gap, for a constant incident radiation wavelength (1.55 μm in this case), power (7.5 mW) and spot radius (27.5 μm, see Fig. 1) for the first three detectable resonance modes. As it is inferred from the results shown in the curves of Fig. 3 and cross-

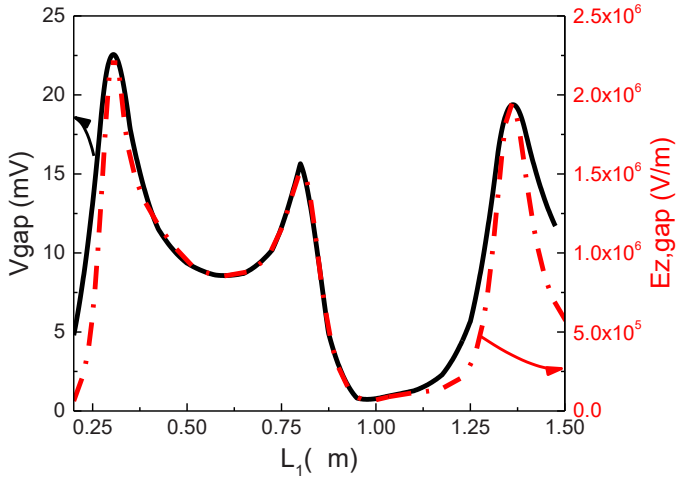

Fig. 3. Voltage and z-component of the electric field in the gap region as a function of dipole length L_1. The three peaks at 300 nm, 810 nm and 1361 nm correspond to the first three detectable resonance modes, which can be identified with the λ/2, 3λ/2 and 5λ/2 modes of a λ/2 dipole structure. Constant parameters of the laser source considered in the calculations are: radiation wavelength λ= 1.55 μm, power P_{in}= 7.5 mW and spot radius SR= 27.5 μm.

section maps of Fig. 4 corresponding to a preliminary analysis, for our proposed dipole nanoantenna, which dimensions are reported in Table 1, the first, second and third resonance detectable modes are found when dipole is approximately 300 nm, 810 nm and 1361 nm long, respectively. In particular, each one of the three peaks observed in the graphs of the gap voltage (V_{gap}) and the electric field in z-direction in the centre point of the dipole nanoantenna gap vs. dipole length (L_1) (Fig. 3) can be identified with the expected patterns of the current density distribution flowing through the nanoantenna metallic part, as shown in Fig. 4.a-c and the z-component of the electric field in the dielectric regions around the metal layer of the nanoantenna, as shown in Fig. 4.d-f Indeed, an examination of the computed current density and electric field distributions indicate that the first three detectable modes correspond to the standard λ/2 (Fig. 4.a,d), 3λ/2 (Fig. 4.b,e) and 5λ/2 (Fig. 4.c,e) dipole antenna modes. Notice, however, that our nanoantenna is not a standard RF dipole antenna, where the total length L (L=2·L1 or L=L1+L2 when consider the non-symmetric case) equals λ/2 in the first resonant mode. In our case, we have a plasmonic nanoantenna in which the wavelength of electromagnetic waves propagating in the metal of the nanoantenna is reduced with respect to the free space propagation. Consequently, the ratio L/(λ/2) which is 1 for a RF antenna, is slightly reduced for a plasmonic one [31,32], as it is verified by our results:

Table 1
Geometry characteristics of cantilevers and nanoantenna.

Parameter	Value	Units
Dipole arm length, (L_{Arm1}/$L_{Arm\ 2}$)	2/2	μm
Dipole width, w_1	0.08	μm
Dipole arm width, w_2	0.1	μm
Dipole length, (L_1/L_2)	1.36/1.36	μm
Dipole gold thickness, (t_{gd})	0.035	μm
Dipole silicon nitride thickness, (t_{dd})	0.14	μm
Cantilever length, (l_c)	200	μm
Cantilever width, (w_c)	28	μm
Cantilever base width, (w_b)	184	μm
Cantilever silicon nitride thickness, (t_{dc})	0.6	μm
Cantilever gold thickness, (t_{gc})	0.07	μm
Capacitive gap, (g_0)	0.01	μm
Overlapping Area, (A)	0.01	μm^2

2·L1/(λ/2)= 600 nm/(1550/2 nm)= 0.77 for the first detectable mode (n = 1), 2·L1/(3λ/2)= 1620 nm/(3·1550 nm/2)= 0.69 for the second detectable mode (n = 3), and 2·L1/(5λ/2)= 2722 nm/(5·1550 nm/2)= 0.70 for the third detectable mode (n = 5). In summary, the results demonstrate that the resonant behaviour of the nanoantenna is highly dependent on the dipole length, with distinct mode profiles observed for each configuration. Additionally, it is observed that the maximum voltage and z-component electric field in the gap region is obtained for the first detectable mode (n = 1), followed by the third (n = 5) and second (n = 3) detectable modes.

3.1. COMSOL optimization

After the previously described preliminary analysis of the V_{gap} and electric field dependence on the dipole nanoantenna length, a refinement of the final design dimensions has been performed through a COMSOL optimization process defining V_{gap} as the variable to be maximized for a radiation wavelength of 1.55 μm. The lengths $L_1 = L_2$ and $L_{Arm1} = L_{Arm2}$ were considered as free parameters for optimization, while the Si_3N_4 thickness was assumed to be fixed at 140 nm, since it is the optimal value from a fabrication point of view as it was demonstrated in a previous work [30]. All simulations of the optimization process were carried out using a laser power of 7.5 mW and a 27.5 μm beam radius. For an initial gap distance fixed at g_0= 10 nm, the set of parameters resulting from an optimization process limited to a range of dipole nanoantenna lengths around the length of the fifth mode is the following: $L_1 = L_2 = 1360$ nm, $L_{Arm1} = L_{Arm2} = 2$ μm, and $W_1 = 80$ nm, $W_2 = 100$ nm. The reason for choosing the 5th mode is that its longer length of 1360 nm allows for an easier fabrication process, at an acceptable tradeoff of a small reduction in V_{gap} and return loss compared to the first mode with a 300 nm dipole length. The optimized dimensions

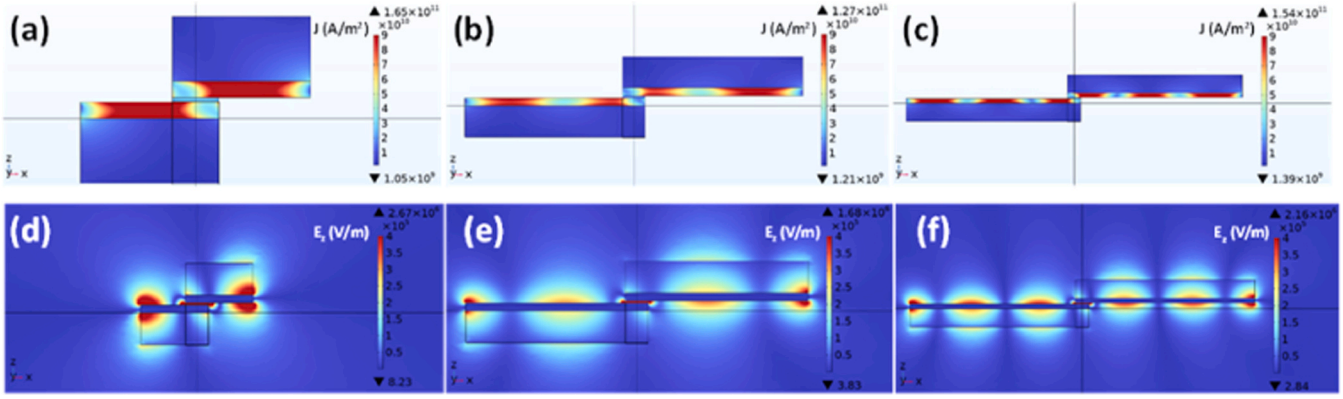

Fig. 4. Maps of the current density (a-c) and z-component of the electric field (d-f), for the first three detectable resonance modes observed when dipole length is 300 nm (a,d), 810 nm (b,e) and 1361 nm (c,f).

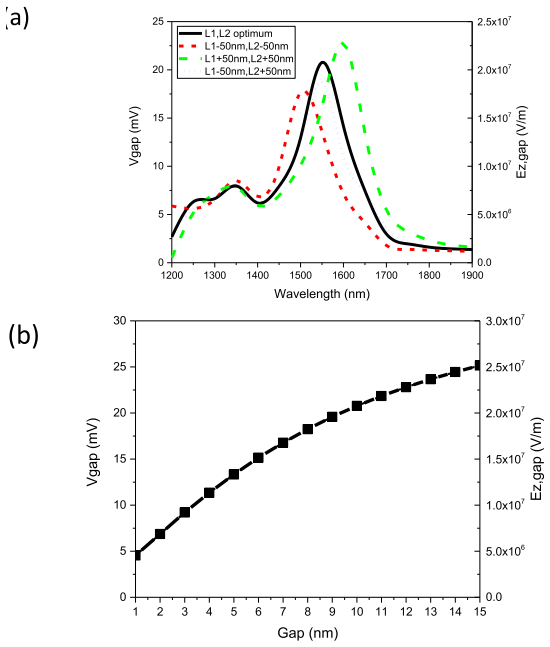

Fig. 5. (a) Spectral response of V_{gap} obtained from COMSOL simulations for L_1 and L_2 at and around the optimum case (L_1=L_2=1360 nm). Gap distance is g_0 = 10 nm. (b) Voltage induced within the feed gap area vs. gap distance. Laser power is P_{in}= 7.5 mW and spot radius is SR= 27.5 μm.

are included in Table I.

In order to quantify the effect of the fabrication tolerance on the response of V_{gap} versus wavelength, simulations for four different values of L_1 and L_2 around the optimal case, with a gap distance g_0= 10 nm were conducted. This analysis considered a 50 nm tolerance limit, reflecting the resolution of the focused ion beam (FIB) milling process used [30]. The results of this analysis summarised in Fig. 5.a demonstrate that simultaneous deviations of L_1 and L_2 by 50 nm in the same direction result in the V_{gap} (and z-direction electric field in the middle of the gap) peak to the right shifting at 1600 nm (for L_1 + 50 nm and L_2+50 nm) or to the left at 1500 nm (for L_1−50 nm and L_2−50 nm), as illustrated by the orange and purple curves in Fig. 5.a, respectively. If the excitation radiation is fixed at 1550 nm and cannot be tuned to match the nanoantenna resonance, the V_{gap}, and correspondingly the z-direction voltage in the middle of the gap, decreases from 21 mV at optimal L_1 and L_2) to approximately 15 mV for both the shortened (L_1−50 nm and L_2−50 nm) and elongated (L_1+50 nm and L_2+50 nm) cases at the excitation wavelength. Additionally, the voltage induced within the feed gap area V_{gap} together with the electrical field in the z direction at the middle point of the gap were analysed as a function of gap distance as presented in Fig. 5.b. It is worth noting that since the z-component of the electric field, $E_{z,gap}$, is not constant along the gap region in the z direction, V_{gap} and gap distance, g, values in the plot of Fig. 5.b are not linearly related by $E_{z,gap}$=V_{gap} /g, as it is evidenced, for instance, by the non-linear V_{gap} vs. gap distance curve. Most importantly, this figure shows that gap voltage decreases as the gap is decreased and that the smaller the gap the faster the gap voltage decreasing rate is.

4. Mechanical response

After settling nanoantenna dimensions and feed gap voltage, the deflection of the microcantilevers, caused by the electrostatic force induced in the transduction gap, has been self-consistently calculated by coupling RF, electrostatics, and solid mechanics COMSOL modules. This deflection was quantified by calculating the displacement at the cantilever's free end. Additionally, to this displacement produced by the optically induced electrostatic force, also called opto-electromechanical (OEM) displacement, we have also considered the parasitic displacement caused by the optically induced heating of the cantilevers and transduced by a bimetallic effect, denoted as opto-thermomechanical (OTM) displacement, combining in this case RF, thermal and solid mechanics COMSOL modules. Both calculations were performed for laser powers ranging from 1 mW to 7.5 mW (the lower and upper limits of our experimental setup) and considering the optimal case (optimal L_1 and L_2) in terms of V_{gap}, an initial gap of g_0= 10 nm and a spot radius of 27.5 μm, corresponding to the beam waist as we have considered the paraxial approximation and a Gaussian beam to describe the focused laser beam. In COMSOL simulations, the NEMSTENNA is placed inside a spherical air-domain simulation box of 345 μm radius, which is large enough to minimize boundary reflections. The outer faces of this domain are assigned scattering boundary conditions in the Electromagnetic Waves module to emulate free-space propagation. Module couplings are setup as follows: the Joule Heating feature of the RF module is used to compute the volumetric power density generated mainly in the gold layer of the NEMSTENNA, which is passed directly to the Heat Transfer in Solids module as a heat source. The resulting temperature rise induces mechanical stress, which is handled by coupling the Heat Transfer module to the Solid Mechanics module via the Thermal Expansion multiphysics node. Then, at each time step of a time-dependent study, the Heat Transfer and Solid Mechanics solvers are coupled, allowing the structure to heat up and deform gradually. To capture the deformation of the NEMSTENNA geometry under thermal expansion, we enable COMSOL's Moving Mesh (Arbitrary Lagrangian–Eulerian) interface. This deformed geometry feature updates the finite-element mesh at each time step based on the computed displacement field, so that the shape of the NEMSTENNA evolves dynamically with temperature.

4.1. Opto-electromechanical (OEM)

Two computational approaches have been evaluated for simulating the OEM displacement induced by near-infrared (IR) laser excitation in the feed gap area of our device: an iterative or feedback method, and a non-iterative one. In the iterative approach, the voltage induced within the feed gap area is recalculated in an RF simulation step, each time the gap distance is reduced by the OEM displacement of the cantilevers (evaluated at their free-end) as calculated in the previous electrostatic and mechanical simulation step. In contrast, the non-iterative method assumes V_{gap} to be constant and independent of changes in gap distance, maintaining its initial value corresponding to the initial gap distance throughout the whole simulation. The findings indicate that at high power levels, the iterative method introduces slight variations in displacement compared to the non-iterative method. Nevertheless, at lower power levels, both methods agree closely in terms of displacement calculations, suggesting that using the non-iterative method to determine displacement values is acceptable within permissible margins of error. Additionally, the iterative method requires more batches of simulations, which implies more computational resources than the non-iterative simple constant sweep approach. In Fig. 6, the displacement values obtained by both calculation methods and the corresponding errors (difference between iterative and non-iterative displacement values) as a function of IR laser power levels are presented. Overall, both iterative and non-iterative methods yield comparable results for laser powers below 3 mW, with negligible differences below 1 pm, and non-negligible discrepancies with a linearly increasing error for laser power levels over 3 mW. For instance, at 7.5 mW IR laser power, the iterative method shows a static deflection of approximately 50 pm, while the non-iterative method shows a displacement of 64 pm, resulting in a deviation error of 14 pm and a relative error of 28 %. In order to relax the computational load, we have used the non-iterative method,

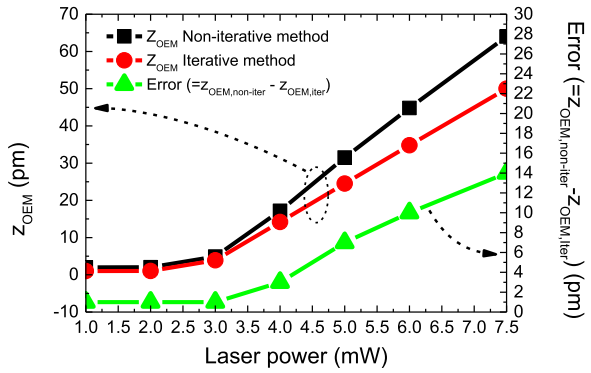

Fig. 6. Static opto-electromchanical OEM deflection calculated with and without the iterative method and the difference between both vs. laser power. Spot radius is SR= 27.5 μm and gap distance is $g_0 = 10$ nm.

keeping in mind that the error grows with the incident power level.

4.2. Opto-thermomechanical (OTM)

In order to analyse the opto-thermomechanical (OTM) transduction mechanism as the parasitic effect that will screen the desired opto-electromechanical (OEM) signal, we have also combined multiple physical domains to couple the interactions between IR light, heat, and mechanical deformation. The COMSOL Multiphysics setup has integrated in this case RF, thermal and solid mechanics domains. The material properties used in the simulations are summarized in Table 2 and also detailed in reference [33]. The properties are inferred from experimental data on the materials' thermal, optical, electrical, and mechanical characteristics. Here, in the EM simulation analysis performed by the RF module the absorption of the optical energy in the material is calculated using Maxwell's equations. Using the refractive index values for Au measured by Johnson and Christy [34], as tabulated in [35], we have calculated with a coherent summation of multiple passes model that the Au surface of our optomechanical nanoantenna device reflects 96.8 % and absorbs about 2.5 % of the total incident power. Only a 0.7 % is transmitted to the Si_3N_4 layer underneath. Subsequently, the thermal module uses as a simulation input the heat generated by the currents as obtained from the RF analysis to calculate the resulting temperature distribution. For this, the heat transfer equations of the thermal COMSOL module consider the effects of conduction, convection and radiation with the corresponding appropriate parameters [33]. It is worth to notice that as the opto-thermomechanical transduction is mainly produced in the body of the triangular microcantilever, the current distribution at the nanoantenna is not contributing to this calculation. Indeed, when we have calculated the thermal distribution and the corresponding opto-thermomechanical OTM response, no significant differences have been found on whether the nanoantenna is present or absent in the simulations.

Table 2
Optical, thermal and mechanical properties of the materials involved in COMSOL simulations.

Property	Au	Si_3N_4	Units
Heat capacity, C_p	129	700	J/(kg·K)
Thermal conductivity, κ	150[a], 230[b]	2.1[c], 4[d]	W/(m·K)
Convective heat transfer coeficient, h	$3.8{\cdot}10^5$	$4{\cdot}10^5$	W/(m²·K)
Thermal Boundary Resistance, TBR	$0.81{\cdot}10^{-8}$	$0.8{\cdot}10^{-8}$	m²·K/W
Surface emissivity, ϵ	0.05	0.5	
Density, ρ	19280	3100	kg/m³
Refractive index, n	0.52406	1.9963	
Extinction coeficient, k	10.742	0	
Electrical conductivity, σ	$45{\cdot}10^6$	0	S/m
CTE, α	$14.1{\cdot}10^{-6}$	$2.3{\cdot}10^{-6}$	K^{-1}
Young's modulus, E	80	250	GPa
Poisson's ratio, ν	0.44	0.23	

[a] Au thickness= 35 nm
[b] Au thickness= 70 nm
[c] Si_3N_4 thickness= 140 nm
[d] Si_3N_4 thickness= 600 nm

Next, the temperature distribution from the thermal analysis is imported into the structural mechanics module. The resulting mechanical deformation is then computed, considering the thermal strain effects. Our optomechanical antenna device is composed of a sandwich of three materials, Au(35 nm)/Si_3N_4(600 nm)/Au(70 nm) (Fig. 1), each one with different coefficients of thermal expansion (CTE) [33]. The asymmetry introduced by the difference in the Au thickness will be the responsible of the cantilever bending by the bimetallic effect. Indeed, the thicker Au layer will suffer a large expansion strain than the thinner one, and the cantilever will bend in the gap closing direction. In order to validate experimentally the COMSOL predictions of OTM parasitic signal, we have measured the opto-thermally induced displacement on a single cantilever component. In the measurement setup, as described in previous works [23,33], focusing of the IR laser beam (Thorlabs SFL1550P current/temperature controlled by ITC4001) is achieved through three different microscope objectives: 100X, 50X and 20X (Mitutoyo M Plan APO SL), that produce 8 μm, 14 μm and 27.5 μm spot radius, respectively. The deflection at the free-end of the cantilever is detected by a red diode laser (Thorlabs CPS670F 670 nm 4.5 mW) coupled to a 4-quadrants position photodetector (New Focus Quadcell Photoreceiver 2901) readout system. The transient signal obtained at the output of the photodetector when IR laser power is switched (OFF-ON-OFF transients) is then analysed by means of an oscilloscope (Tektronix MDO3024). The stationary deflection signal difference between the ON and OFF states (in terms of cantilever free-end displacement) for different laser power levels is obtained as presented in Fig. 7.

As illustrated in this figure, there is an excellent agreement between COMSOL model predictions and experimental values.

Finally, in the last analysis which consisted of comparing the OEM signal with the OTM parasitic, we have used a figure of merit (FoM) simply defined as the ratio between the OEM and the OTM induced vertical displacements of the cantilevers fre-end (z): $FoM=z_{OEM}/z_{OTM}$. The as defined FoM has been then evaluated for the three different achievable laser spot radii, i.e. 8, 14 and 27.5 μm and represented together with both displacements (OEM and OTM) in Fig. 8. Here, we observe that as laser beam radius decreases from 27.5 μm to 8 μm, OTM parasitic decreases from 25 nm to 0.7 nm because the area illuminated of the cantilever decreases too, OEM increases from 50 pm to 150 pm

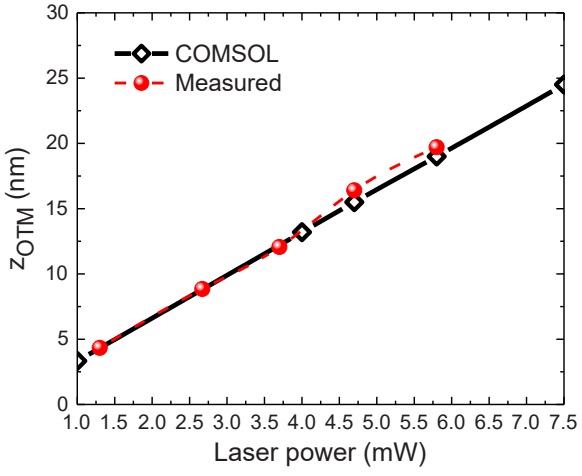

Fig. 7. Experimental and COMSOL simulated steady state displacement of the cantilever free-end in out-of-plane direction, z, after laser power OFF-ON switching transient for different laser powers ranging from 1 to 7.5 mW. Spot radius is SR= 27.5 μm and gap distance is $g_0 = 10$ nm.

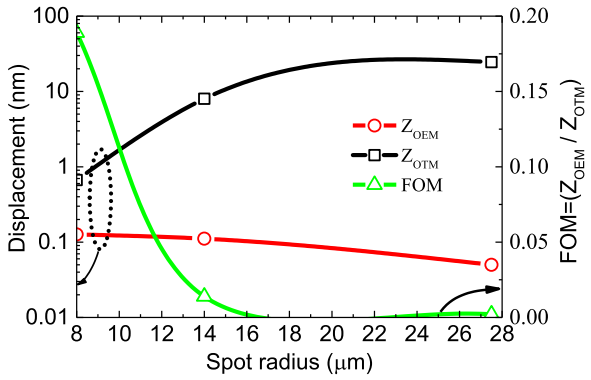

Fig. 8. OEM and OTM displacements and their corresponding OEM/OTM ratio as defined by the FoM as a function of the laser spot radii, ranging from 8 to 27.5 μm. Laser power is P_{in}= 7.5 mW and gap distance is g_0 = 10 nm.

because the power density in the nanoantenna region is increased, thereby maximizing the opto-electromechanical effect and minimizing the opto-thermomechanical parasitic. Consequently, the FoM is increased from $2{\cdot}10^{-3}$ to 0.2, which means an enhancement of two orders of magnitude. Since both OTM and OEM dependences on the spot radius are non-linear, and OTM decreases much faster than OEM grows when spot radius is decreased, the FoM and its rate of change grows very significantly when spot radius is approaching 8 μm. The marginal change in the FoM underscores the need for improved design geometry to achieve higher performance. Future research should focus on reducing the opto-thermomechanical parasitic effect but specially on enhancing the opto-electromechanical transduction signal.

5. Conclusion

In this study we have demonstrated that the parasitic opto-thermomechanical response (OTM) substantially impacts the performance of the optomechanical naoantenna device, overshadowing the intended opto-electromechanical (OEM) response. Experimental validation of the OTM displacement component closely matches our COMSOL Multiphysics simulations, confirming the influence of localized heating on the microcantilever's deflection. To improve the overall performance and FoM of the device, future work will focus on optimizing the design geometry. This optimization aims to reduce the undesired slow but large amplitude response of the OTM effect, while enhancing the fast OEM response, thereby advancing towards a practical application of optomechanical antenna devices in NIR radiation detection.

CRediT authorship contribution statement

Khoshmaram Daniyal: Writing – original draft, Visualization, Validation, Software, Resources, Methodology, Investigation, Formal analysis, Data curation, Conceptualization. **Gabriel Abadal:** Writing – review & editing, Validation, Supervision, Project administration, Investigation, Formal analysis, Conceptualization. **Garcia Joan Garcia:** Writing – review & editing, Validation, Methodology. **Xavier Cartoixà:** Writing – review & editing, Supervision, Software, Funding acquisition.

Declaration of Competing Interest

The authors declare the following financial interests/personal relationships which may be considered as potential competing interests: Xavier Cartoixa reports financial support was provided by Spain's ministry of science and innovation. If there are other authors, they declare that they have no known competing financial interests or personal relationships that could have appeared to influence the work reported in this paper.

Acknowledgements

This work was funded by Spain's Ministerio de Ciencia e Innovación under Grant No. PID2021-127840NB-I00 (MICINN/AEI/FEDER, UE).

Data availability

Data will be made available on request.

References

[1] K.E. Petersen, Silicon as a mechanical material, Proc. IEEE 70 (5) (1982) 420–457, https://doi.org/10.1109/PROC.1982.12331.
[2] R. Hajare, V. Reddy, R. Srikanth, MEMS based sensors – a comprehensive review of commonly used fabrication techniques, Mater. Today Proc. 49 (2021), https://doi.org/10.1016/j.matpr.2021.05.223.
[3] F. Ghazali, M. Hasan, T. Rehman, M. Nafea, M.S. Mohamed Ali, K. Takahata, MEMS actuators for biomedical applications: a review, J. Micromech. Microeng. 30 (2020) 73001–73020, https://doi.org/10.1088/1361-6439/ab8832.
[4] H. Sun, M. Yin, W. Wei, J. Li, H. Wang, X. Jin, MEMS based energy harvesting for the Internet of things: a survey, Microsyst. Technol. 24 (2018), https://doi.org/10.1007/s00542-018-3763-z.
[5] L. Ni, R.M. Pocratsky, M.P. de Boer, Demonstration of tantalum as a structural material for MEMS thermal actuators, Microsyst. Nanoeng. 7 (1) (2021) 6, https://doi.org/10.1038/s41378-020-00232-z.
[6] D. Thuau, C. Ayela, P. Poulin, I. Dufour, Highly piezoresistive hybrid MEMS sensors, Sens. Actuators A Phys. 209 (2014) 161–168, https://doi.org/10.1016/j.sna.2014.01.037.
[7] G. Pillai, S.-S. Li, Piezoelectric MEMS resonators: a review, IEEE Sens. J. 21 (11) (2021) 12589–12605, https://doi.org/10.1109/JSEN.2020.3039052.
[8] S. Nabavi, M. Ménard, F. Nabki, A SOI out-of-plane electrostatic MEMS actuator based on in-plane motion, J. Micro Syst. 31 (5) (2022) 820–829, https://doi.org/10.1109/JMEMS.2022.3190829.
[9] M. Moczała, et al., Technology of thermally driven and magnetomotively detected MEMS microbridges, Sens. Actuators A Phys. 240 (2016) 17–22, https://doi.org/10.1016/j.sna.2016.01.041.
[10] J.-C. Chiou, C.-C. Hung, C.-Y. Lin, Design, fabrication and actuation of a MEMS-based image stabilizer for photographic cell phone applications, J. Micromech. Microeng. 20 (7) (2010) 75025, https://doi.org/10.1088/0960-1317/20/7/075025.
[11] B. Padha, I. Yadav, S. Dutta, S. Arya, Recent developments in wearable NEMS/MEMS-based smart infrared sensors for healthcare applications, ACS Appl. Electron. Mater. 5 (10) (2023) 5386–5411, https://doi.org/10.1021/acsaelm.3c00860.
[12] R.N. Dean, A. Luque, Applications of microelectromechanical systems in industrial processes and services, IEEE Trans. Ind. Electron 56 (4) (2009) 913–925, https://doi.org/10.1109/TIE.2009.2013691.
[13] X. Guo, W. Yang, X. Xiong, Z. Wang, X. Zou, MEMS reservoir computing system with stiffness modulation for multi-scene data processing at the edge, Microsyst. Nanoeng. 10 (1) (2024) 84, https://doi.org/10.1038/s41378-024-00701-9.
[14] Y. Yoon, I.-J. Cho, A review of human augmentation and individual combat capability: focusing on MEMS-based neurotechnology, Micro Nano Syst. Lett. 12 (1) (2024) 17, https://doi.org/10.1186/s40486-024-00205-1.
[15] T. Xu, J. Sun, H. Wu, H. Li, H. Li, Z. Tao, 3D MEMS in-chip solenoid inductor with high inductance density for power MEMS device, IEEE Electron Device Lett. 40 (11) (2019) 1816–1819, https://doi.org/10.1109/LED.2019.2941003.
[16] K. Entesari, G.M. Rebeiz, A 12-18-GHz three-pole RF MEMS tunable filter, IEEE Trans. Microw. Theory Tech. 53 (8) (2005) 2566–2571, https://doi.org/10.1109/TMTT.2005.852761.
[17] K. Shih, et al., Active MEMS metamaterials for THz bandwidth control, Appl. Phys. Lett. 110 (16) (2017) 161108, https://doi.org/10.1063/1.4980115.
[18] G. Zhou, Z.H. Lim, Y. Qi, G. Zhou, Single-pixel MEMS imaging systems, Micromachines 11 (2) (2020), https://doi.org/10.3390/mi11020219.
[19] G. Demirhan Aydin, O.S. Akar, T. Akin, Wafer level vacuum packaging of MEMS-based uncooled infrared sensors, Micromachines 15 (8) (2024), https://doi.org/10.3390/mi15080935.
[20] K. Jensen, J. Weldon, H. Garcia, A. Zettl, Nanotube radio, Nano Lett. 7 (2007) 3508–3511, https://doi.org/10.1021/nl0721113.
[21] Y. Cui, et al., A survey of mechanical antennas applied for low-frequency transmitting, iScience 26 (1) (2023) 105832, https://doi.org/10.1016/j.isci.2022.105832.
[22] N. Barani, K. Sarabandi, Mechanical antennas: emerging solution for Very-Low frequency (VLF) communication. 2018 IEEE International Symposium on Antennas and Propagation & USNC/URSI National Radio Science Meeting, 2018, pp. 95–96, https://doi.org/10.1109/APUSNCURSINRSM.2018.8608412.
[23] R. Ruiz, G. Abadal, Remote dynamic actuation of an electrostatically driven microcantilever by a wireless power transfer system, Sens. Actuators A Phys. 345 (2022) 113798, https://doi.org/10.1016/j.sna.2022.113798.
[24] R. Ruiz, G. Abadal, Direct transduction from radiofrequency radiated power to static and dynamic flexural mechanical modes, 2021 21st International Conference

on Solid-State Sensors, Actuators and Microsystems (Transducers) (2021) 144–147, https://doi.org/10.1109/Transducers50396.2021.9495668.
[25] R. Ruiz, J. Bonache, G. Abadal, A flexible dipole antenna for direct transduction of microwave radiated power into DC mechanical deflection, Sens. Actuators A Phys. 340 (2022) 113536, https://doi.org/10.1016/j.sna.2022.113536.
[26] C. Belacel, Y. Todorov, S. Barbieri, D. Gacemi, I. Favero, C. Sirtori, Optomechanical terahertz detection with single meta-atom resonator, Nat. Commun. 8 (1) (2017) 1578, https://doi.org/10.1038/s41467-017-01840-6.
[27] Y. Zhang, S. Hosono, N. Nagai, K. Hirakawa, Novel bolometric THz detection by MEMS resonators, 2018 43rd International Conference on Infrared, Millimeter, and Terahertz Waves (IRMMW-THz) (2018) 1–2, https://doi.org/10.1109/IRMMW-THz.2018.8510488.
[28] Y. Zhang, S. Hosono, N. Nagai, S.-H. Song, K. Hirakawa, Fast and sensitive bolometric terahertz detection at room temperature through thermomechanical transduction, J. Appl. Phys. 125 (15) (2019) 151602, https://doi.org/10.1063/1.5045256.
[29] Y. Zhang, B. Qiu, N. Nagai, M. Nomura, S. Volz, K. Hirakawa, Enhanced thermal sensitivity of MEMS bolometers integrated with nanometer-scale hole array structures, AIP Adv. 9 (8) (2019) 85102, https://doi.org/10.1063/1.5113521.
[30] D.K. Maram, X. Borrisé, J. Garcia-Garcia, R. Ruiz, X. Cartoixà, G. Abadal, Design and fabrication of an opto-mechanical antenna in the NIR range, Micro Nano Eng. 23 (2024) 100241, https://doi.org/10.1016/j.mne.2024.100241.
[31] R. Esteban, et al., Direct Near-Field optical imaging of higher order plasmonic resonances, Nano Lett. 8 (10) (2008) 3155–3159, https://doi.org/10.1021/nl801396r.
[32] A.F. McKinley, T.P. White, K.R. Catchpole, Theory of the circular closed loop antenna in the terahertz, infrared, and optical regions, J. Appl. Phys. 114 (4) (2013) 44317, https://doi.org/10.1063/1.4816619.
[33] D.K. Maram, X. Cartoixá, G. Abadal, Analysis of the photothermal parasitic effect on an optomechanical antenna, 2024 IEEE Sensors (2024) 1–4, https://doi.org/10.1109/SENSORS60989.2024.10785153.
[34] P.B. Johnson, R.W. Christy, Optical constants of the noble metals, Phys. Rev. B 6 (12) (1972) 4370–4379.
[35] Polyanskiy, M.N., Refractive index database, (n.d.), ⟨https://refractiveindex.info⟩.

Daniyal Khosh Maram received the M.Sc. (with Hons.) degree in electrical engineering (nano and microelectronics) from the Amirkabir University of Technology (Tehran Polytechnic), Tehran, Iran, in 2020. He is currently working toward the Ph.D. degree in electrical engineering with the Department of Electronics and Telecommunication Engineering, Universidad Autónoma de Barcelona (UAB), Bellaterra, Spain. His research interests include nanoantennas, plasmonic structures, optoelectronic devices, device physics, and nanoelectromechanical systems.